

# Mechanical Instabilities of Individual Multiwalled Carbon Nanotubes under Cyclic Axial Compression

Hsao W. Yap,<sup>†,§</sup> Roderic S. Lakes,<sup>‡</sup> and Robert W. Carpick<sup>\*,†,§</sup>

*Department of Physics, Department of Engineering Physics, Materials Science Program, and Rheology Research Center, University of Wisconsin—Madison, Madison, Wisconsin 53706*

*Received November 26, 2006; Revised Manuscript Received February 14, 2007*

## ABSTRACT

Individual multiwalled carbon nanotubes with a range of aspect ratios are subjected to cyclic axial compression to large strains using atomic force microscopy. Distinct elastic buckling and postbuckling phenomena are observed reproducibly and are ascribed to Euler, asymmetric shell buckling (i.e., kinking), and symmetric shell buckling. These show agreement with continuum theories that range from approximate to remarkable. Shell buckling yields reproducible incremental negative stiffness in the initial postbuckled regime.

It is well-known that carbon nanotubes (CNTs) exhibit excellent mechanical properties<sup>1</sup> with remarkable reversibility under large deformations.<sup>2,3</sup> Under axial compression, various mechanical instabilities like Euler buckling<sup>4</sup> and shell buckling, either asymmetric (i.e., kinking) or symmetric,<sup>5</sup> can occur with macroscopic tubes. As with macroscopic tubes and shells, the initial post-shell buckling regimes for axially compressed CNTs can possess incremental negative stiffness, where the axial force decreases as the axial compressing increases over a range of displacements. This is seen in the axial compression of single-walled (SW) CNTs using molecular dynamics (MD) and finite element (FE) simulations.<sup>6–8</sup> Force–displacement plots derived from MD simulations also exhibited negative stiffness due to reversible kink deformation of CNTs indented on stiff surfaces.<sup>9</sup> One general aspect of negative stiffness, as shown recently by Lakes et al.,<sup>10</sup> is the possibility of greatly enhanced overall stiffness and damping (internal friction) of a composite system due to negative stiffness inclusions, including rendering a tin matrix with barium titanate inclusions stiffer than diamond.<sup>11</sup> Therefore, it is desirable to determine the precise conditions (loading and boundary conditions, CNT dimensions, resulting critical loads, and repeatability) under which CNTs exhibit negative stiffness and, eventually, to design CNT-based composites that take advantage of this behavior.

There is only one experimental report in the literature of an axial compression experiment on multiwalled carbon

nanotubes (MWCNTs) exhibiting a negative stiffness force drop.<sup>12</sup> The force drop is correlated with the formation of a series of asymmetric local buckles (kinking) on the CNT, as demonstrated by simultaneous, in situ transmission electron microscopy (TEM). However, only a handful data points were taken. As such, changes of force over small increments in displacements cannot be identified and analyzed. Force drops due to symmetric shell buckling<sup>5</sup> have also not been experimentally observed in individual MWCNTs at all. Previous axial compression tests on large aspect ratio (length/radius = 150–750) MWCNTs and carbon nanosprings attached to atomic force microscopy (AFM) cantilevers<sup>13–15</sup> did not yield force drops initially because Euler buckling occurred instead of shell buckling. The work of Waters et al.<sup>16</sup> is the first report to claim supposed occurrence of symmetric shell buckling in the axial compression of a single, low aspect ratio (1–2) MWCNT under a nanoindenter, but no force drops were observed, possibly because the MWCNTs were too short.<sup>3</sup>

Here, we examine in detail axial buckling instabilities and conditions for observing negative stiffness behavior of individual MWCNTs under cyclic axial compression. Force–displacement plots were obtained using a Digital Instruments (DI) Multimode AFM at 1–2 Hz cycling frequencies. AFM is used because it provides not only superb force-sensing capabilities but also reasonably high spatial resolution. Silicon contact mode AFM probes (with experimentally determined spring constants<sup>17</sup> of 0.15–0.4 N/m) with thermal chemical vapor deposition grown MWCNTs mounted on the tips (CNTek Probe, Nanoscience Instruments) were used for one set of experiments. The tubes are attached via electron beam induced decomposition,<sup>18</sup> and we consider it to be a

\* Corresponding author. E-mail: carpick@seas.upenn.edu.

<sup>†</sup> Department of Physics.

<sup>‡</sup> Department of Engineering Physics, Materials Science Program, and Rheology Research Center.

<sup>§</sup> Current address: University of Pennsylvania, Philadelphia, PA 19104.

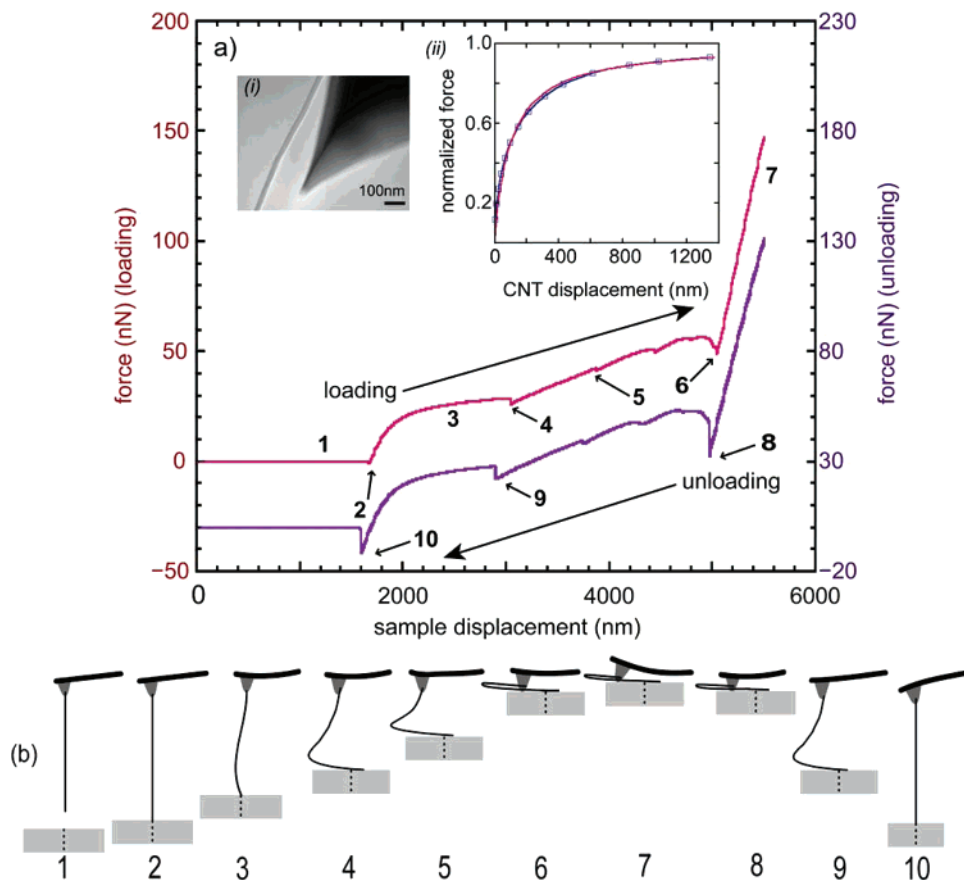


**Figure 1.** (a) Force vs sample displacement plot of an AFM tip-mounted MWCNT (aspect ratio  $\sim 220$ ) under cyclic axial loading. The unloading curve has been translated down by 40 nm for clarity. Inset i: TEM image of the MWCNT. Inset ii: curve fit (blue line with open squares) to the experimental data of the Euler buckling region (red line). (b) Proposed events: (1) CNT out of contact. (2) CNT snaps into contact. (3) CNT Euler buckles. (4) Another snap in. (5) CNT slips. (6) Tip snaps in. (7) Cantilever bends upward. (8) Cantilever/tip retracts and pulls off. (9 and 10) CNT pulls off. (Note: Eccentric loading and initial imperfection not taken into account.)

“fixed” mechanical boundary condition (able to resist translation and rotation). Inset i of Figure 1a is a transmission electron microscopy (TEM) image of a tip-mounted MWCNT, where the outer diameter and wall thickness of the MWCNT are  $30 \pm 2$  and  $10 \pm 2$  nm respectively. Inset i of Figure 2a is a SEM image of another tip-mounted MWCNT. These MWCNTs had aspect ratios ranging from 80 to 220. For a second set of experiments, an array of free-standing, vertically aligned multiwalled carbon nanostructures were grown from the pores of an anodized aluminum oxide (AAO) template via hot filament dc plasma enhanced chemical vapor deposition.<sup>19</sup> Some of the structures have angled walls and therefore are classified as multiwalled carbon nanofibers (CNFs). The pores, as well as the columns of Ni catalyst in them, provide a fixed mechanical boundary condition, making them ideal for mechanical loading experiments. Inset i of Figure 3a is a TEM image of one of these MWCNFs. The diameter and wall thickness of this MWCNF are  $80 \pm 2$  and  $30 \pm 2$  nm, respectively. Inset ii of Figure 3a is a three-dimensional rendering of an AFM image of a  $5 \times 5 \mu\text{m}^2$  area of the sample, showing the multiple, individually resolvable MWCNT/Fs.<sup>20</sup> These structures have lower aspect ratios than the tip-mounted MWCNTs, ranging from 20 to 50.

Figure 1a shows a representative force vs sample displacement plot of the axial compression of a high aspect ratio

( $\sim 220$ ) MWCNT attached to an AFM tip, making contact with a Si substrate.<sup>21</sup> In region (1), the MWCNT is out of contact with the sample. At (2), the lever deflects as the MWCNT snaps into contact with the sample. In region (3), a nonlinear response is observed. The nonlinear portion is highly reproducible for both the approach and retract portion, for three different long aspect ratio MWCNTs. As the compression increases, we observe what resembles another snap-in event at (4). This is consistent with another segment of the MWCNT jumping into contact with the sample, perhaps made possible by bending of the CNT. At (5), we observe a series of small dips in the force curve. We propose that these are possible signatures of slippage of the CNT along the Si surface. Finally, a larger snap-in observed at (6) and the force curve increases rapidly and smoothly thereafter in a linear manner (7). This must be due to the tip being in contact with the sample since the slope of this region is equal to the stiffness of the AFM cantilever. The unloading portion matches the loading portion, except that the pull-off events seen at (8), (9), and (10) involve larger force changes than the pull-in events (2), (4), and (5), as expected for any adhesive interaction.<sup>22</sup> This behavior, during cyclic loading and unloading, was reproducible for hundreds of cycles.

The assignment of the initial behavior to Euler buckling can be supported quantitatively, as first shown here. As a first approximation, we use continuum Euler buckling theory<sup>4</sup>

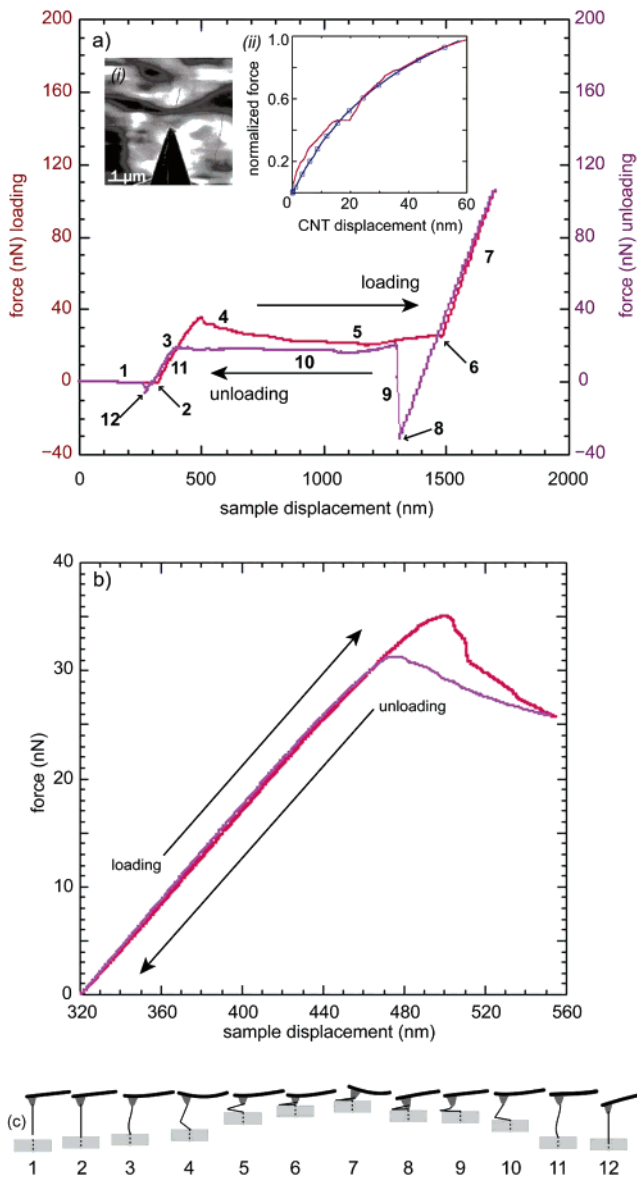


**Figure 2.** (a) Force vs sample displacement plot of another tip-mounted MWCNT (aspect ratio  $\sim 80$ ) under cyclic axial loading. Inset i: SEM image of the MWCNT. Inset ii: curve fit (blue line with open squares) of the Euler buckling (pre-kinking) region (3) of (a) (red line). (b) Region of transition to the kinking regime. (c) Proposed events: (1–3) See Figure 1b. (4) CNT kinks. (5) CNT bends further. (6) Tip snaps in. (7) Cantilever bends upward. (8 and 9) Cantilever/tip retracts and pulls off. (10) CNT springs back and unbends. (11) CNT unbuckles to straight configuration. (12) CNT pulls off. (Note: Eccentric loading and initial imperfection not taken into account.)

to fit the load–displacement data in Figure 1a, region (3). A more precise analysis would account for large transverse deflections and geometric nonlinearities, but doing so results only in marginal differences and only at extreme loads.<sup>4,23</sup> Herein also lies the assumption that any applied transverse force acting on the MWCNT, e.g., due to the tilt angle of the cantilever, is not significant and thus will not affect adversely the analysis below. Following the procedure set out in ref 23, the classical flexural beam equation is used, together with eccentric loading and/or initial imperfection

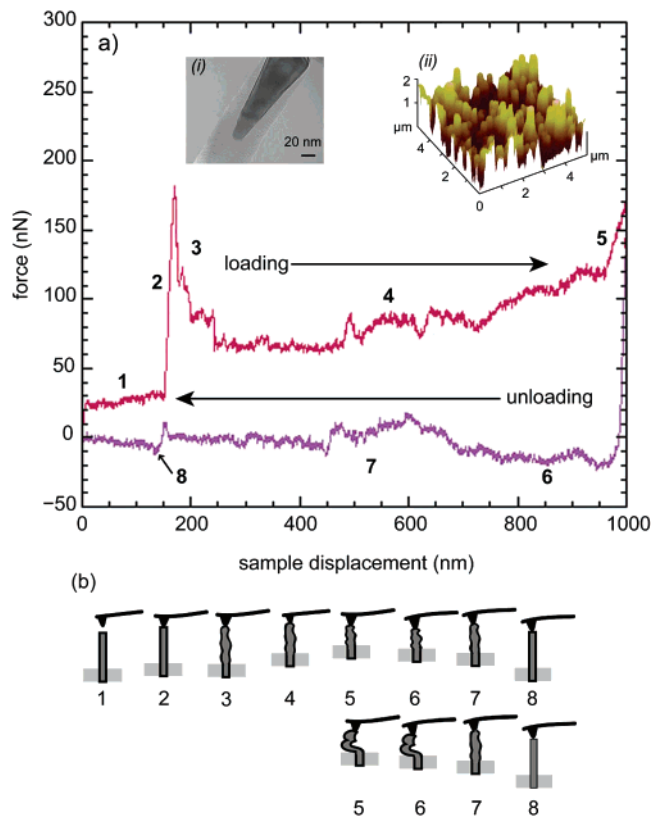


**Figure 3.** (a) Force vs sample displacement plot of a MWCNT/F (aspect ratio 18–45) grown from the AAO pore template under cyclic axial loading. Inset i: representative TEM image of one of these MWCNT/Fs. Inset ii: AFM topographic image of the sample of the vertically aligned MWCNT/Fs. (b) Proposed events: (1–3) See Figure 1b. (4) CNT/F’s initial post-buckling path. After that, CNT/F undergoes either of two post-buckling paths. Top: (5) CNT/F poses resistance (still upright). Bottom: (5) CNT/F poses resistance (other buckled or bent configurations). (6) Tip retracts and CNT starts unbuckling/unbending. (7) Further unbuckling. (8) CNTs predeformed configuration.

taken into consideration. With the appropriate boundary conditions, we solve for the lateral deflection of the MWCNT. Then we relate the lateral deflection to the axial deformation. An equation of force vs axial displacement can be obtained. A least-squares fit of this equation to region (3) of Figure 1a is made. Both eccentric loading and initial geometric imperfection (either a half-sine or a parabolic shape, to account for the initial curvature) of the MWCNT are the only free parameters. Equations for hinged–hinged boundary conditions are given in ref 23. Here, we modified the equations to model hinged–hinged, fixed–free, and fixed–hinged boundary conditions. The latter gave the best fits and make physical sense given the fixed bond between the MWCNT and the tip. Refer to Supporting information for more technical details and physical explanation of terms used. Figure 1, inset ii, shows the excellent curve fit of the normalized force (force/critical buckling force) vs MWCNT displacement.<sup>21</sup> Significant eccentric loading ( $1.04 \mu\text{m}$ ) but only a small half-sine initial imperfection ( $50.3 \text{ nm}$  amplitude) are used for the fit. Figure 1b is a schematic that illustrates the proposed configuration of the MWCNT in each region.

The continuum formula for the critical Euler buckling load of a column is<sup>4</sup>

$$F_{\text{cr}} = \alpha \frac{\pi^2 EI}{L^2} = \alpha \frac{\pi^3 E(R_o^4 - R_i^4)}{4L^2} \quad (1)$$

where  $F_{\text{cr}}$  is the critical buckling load,  $E$  is the Young's modulus of the column,  $I$  is the lesser of the two principal cross sectional moments of inertia about the column's transverse axes ( $= \pi(R_o^4 - R_i^4)/4$  for a hollow cylinder),  $L$  is the column's length,  $\alpha$  is a nondimensional factor that depends on the boundary conditions, and  $R_o$  and  $R_i$  are the outer and inner radii of the column, respectively, assuming it is a hollow tube. We set  $\alpha = 2.04082$  (fixed-hinged boundary condition) and use experimental values of  $L$  (from TEM and AFM),  $F_{\text{cr}}$  (from the force-displacement data), and  $R_o$  and  $R_i$  (from TEM, inset i of Figure 1a). The latter two quantities give  $I = 3.9 \times 10^{-32} \text{ m}^4$ . From eq 1 we obtain the flexural stiffness  $EI = 2.05 \times 10^{-20} \text{ N m}^2$ , and thus  $E = 526 \text{ GPa}$ . This is comparable to measurements of MWCNTs obtained in other experiments.<sup>12,24,25</sup> The high qualities of the fit as well as the reasonable value of  $E$  extracted indicate that our hypothesis of Euler buckling coupled with occurring in region 3 is valid.

Figure 2a shows a representative force vs piezoelectric displacement plot of the axial compression of a moderate aspect ratio (80) MWCNT attached to an AFM tip. The initial out-of-contact region (1) is followed by the usual snap-in event (2), then a slightly nonlinear increase in force (3). The nonlinearity is evident upon closer inspection, as shown in inset ii, again highly consistent with Euler buckling. Then, abruptly (and far sooner than for the high aspect ratio MWCNT), a negative stiffness region (4) begins. The instability seen at (4) is reproducible and is consistent with the mechanics of kinking.<sup>7,9,12</sup> It is observed here and not in Figure 1a because the aspect ratio of this MWCNT is much less here. Kinking, and hence negative stiffness, is therefore dependent on the aspect ratio of the MWCNT. As the displacement is increased further, the CNT compresses further and the force curve plateaus for a substantial displacement range (5). This is consistent with the hypothesis that the lower segments of the MWCNT (after kinking) are slowly adhering to the sample, where this deformed configuration of the CNT poses only slight resistance to the tip. The tip then snaps into contact with the sample at (6). A linear increase in region (7) then occurs. As with Figure 1a, this is due to the tip making contact with the sample as the slope of this region is equal to the stiffness of the AFM cantilever. Therefore we hypothesize that the CNT is fully bent over in this regime. The sample displacement is then reversed, and the linear retraction occurs as with Figure 1. The instability at (8) and the sharp rise at (9) are emblematic of the tip itself pulling out of contact from the sample, while the end of the CNT remains in contact. Then, the MWCNT quickly unbends and springs back up. The hysteresis between the loading and unloading curves in region (10) indicates adhesive forces at work between the lower portion of the

MWCNT and the substrate.<sup>13</sup> In the slightly nonlinear region (11), the MWCNT starts to unbuckle and returns to its straight configuration. The tip finally pulls out of contact with the sample at (12). Figure 2b illustrates the MWCNT's configuration in each region that we hypothesize, based on the force-displacement data.

Figure 2c is a subsequent measurement with the same CNT, where the displacement direction was reversed shortly after the kink event. The resulting negative stiffness feature, as well as that of Figure 2a, was highly reproducible up to thousands of cycles. This demonstrates for the first time that all severe deformations of the MWCNTs, including negative stiffness force drops, are still within the reversible, elastic regime. This is in sharp contrast to the results of ref 12, where cyclic reproducibility is not observed. Once again, the initial portion of the force-displacement plot can be described as a first approximation by Euler buckling.<sup>7,9,12</sup> Following the procedure described above for the high aspect ratio MWCNT, the best curve fit (Figure 2a, inset ii) is again obtained with fixed-hinged boundary conditions as expected. The best fit occurs for eccentric loading of 70 nm and a parabolic initial imperfection of amplitude 104 nm. From the fit,  $EI = 2.35 \times 10^{-21} \text{ N m}^2$ . This is an order of magnitude smaller than  $EI$  obtained in Figure 1a. However, we do not know  $R_o$  and  $R_i$  here, and the strong dependence of  $I$  on  $R$  prevents us from concluding whether or not the value of  $E$  is within reasonable bounds.

Figure 3a is a force vs sample displacement measurement<sup>26</sup> of the axial compression of a MWCNT/F grown from the AAO pores. The length is determined to be  $1.36 \mu\text{m}$  by using AFM to measure the height from the top of the CNT/CNF to the substrate. The exact diameter of this MWCNT/F cannot be determined because of tip convolution, but we can determine an upper limit of 150 nm and a lower limit of 60 nm.<sup>20</sup> The loading phase consists of the initial out-of-contact portion (1), a linear increase in force when MWCNT/F comes into contact with the tip and presumably remains vertical (2), a series of drops in force (negative stiffness) to a low but nonzero value (3), a plateau in the force curve where very little additional force is needed to deform the MWCNT/F (4), and finally a second increase in the force (5). The large hysteresis between the loading and unloading curves could indicate adhesive forces at work or the intrinsic viscoelastic nature of the postbuckled configuration. Some hysteresis has also been reported in MD simulations of axial loading and unloading of SWCNTs.<sup>27</sup> The tip finally pulls off from the MWCNT/F at (8). Figure 3b shows the proposed configurations of the MWCNT/F based on these observations and on the discussion below.

The behavior in Figure 3a is cyclically repeatable (number of reversible cycles varied from 20 to 600), unlike that of Waters et al.'s results. This bifurcation feature slowly fades away with further loading. The behavior is sensitive to the initial loading conditions. We found that 10 out of 50 different MWCNT/Fs exhibited this form of shell buckling with negative stiffness. The rest of the MWCNT/Fs exhibited phenomena possibly attributable to bending or Euler buckling

and will be discussed in detail separately.<sup>28</sup> No signs of brittle fracture of the MWCNT/Fs are observed in scanning electron microscopy (SEM) images of the regions that were tested, though plastic deformation unobservable by SEM could have occurred. The low strain force–displacement behavior (regions 2 and 3) of Figure 3a is qualitatively similar to that for symmetric shell buckling of continuum thin circular cylindrical shells<sup>5</sup> and for CNTs.<sup>6</sup> For a SWCNT undergoing symmetric shell buckling, standard elastic thin shell theory using the Donnell equations can be applied.<sup>7,29</sup> Ru developed a continuum-based multiwall model for axial shell buckling that includes the van der Waals interaction between the walls.<sup>30</sup> The critical buckling strain is approximately independent of thickness and Ru asserts this can be physically justified by considering the ultralow friction and easy sliding between the walls.<sup>31</sup> Using the dimensions of the MWCNT/Fs,<sup>20</sup> the critical strain is given by (eq 32 of ref 30)

$$\epsilon_{cr} = \frac{DL^2}{Ehm^2\pi^2} \sum_{k=1}^N \left( \frac{m^2\pi^2}{L^2} + \frac{n^2}{R_k^2} \right)^2 + \frac{m^2\pi^2 \sum_{k=1}^N \frac{1}{R_k^2}}{L^2 \sum_{k=1}^N \left( \frac{m^2\pi^2}{L^2} + \frac{n^2}{R_k^2} \right)^2} \quad (2)$$

where  $D$  is the bending stiffness,  $h$  is the effective thickness ( $D/Eh \sim 0.02 \text{ nm}^2$ ),<sup>7</sup>  $m$  and  $n$  are the axial half wave and circumferential wave numbers of the periodic buckling pattern, respectively, and the sum is over the radii of all  $N$  walls of a MWCNT/F.<sup>30</sup> Here, we use a total wall thickness of 31 nm,<sup>20</sup> thus  $N = 88$  assuming an interwall spacing of 0.34 nm. Minimizing (2) with respect to  $m$  and  $n$  gives us a theoretical critical strain of 1.70%. This compares surprisingly well with the average experimental value of 1.68%<sup>32</sup> and indicates that the Donnell equations are still approximately applicable for MWCNT/Fs with aspect ratios of  $\sim 35$  too, contrary to just  $\sim 15$  for SWCNTs. This is in stark contrast to Waters et al.'s results,<sup>16</sup> where a clear comparison of the buckling strains could not be made because of tip and substrate compliances and the possibility of sliding along the CNT–substrate interfaces. Also, since they used nanoindenter tips, a few MWCNTs are contacted under large compressive strains. This hinders them from observing the post-shell buckling responses of individual MWCNTs. A more accurate analysis of our results would involve the Flugge equations of cylindrical shells, where the contribution of tangential (axial and circumferential) external forces to equilibrium is not negligible.<sup>33</sup>

The value of  $EA$  can be obtained through the relation  $kL = EA$ , where  $k$  is the normal stiffness of the MWCNT/F derived from the linear elastic region (region 2) of Figure 3a (cantilever stiffness is subtracted away). Using the average values of  $k$  and  $L$ <sup>34</sup>, we obtain  $EA = 1.22 \times 10^{-5} \text{ N}$ . We obtain a lower bound for  $E$  of 22.6 GPa by assuming the maximum possible value of the cross sectional area  $A = \pi(R_o^2 - R_i^2)$ .<sup>20</sup> This assumes that the MWCNT/F has a solid, uniform cross section and is an overestimate of  $A$ , since the

equivalent continuum structure of a MWCNT/F could involve free space between the walls (the true thickness of individual walls in a MWCNT is still not well defined).<sup>7,29,34</sup> We then calculate  $I$  using the same values of  $R_o$  and  $R_i$ . Assuming fixed–hinged boundary conditions, and using the lower bound value for  $E$ , we obtain a lower bound on the critical Euler buckling load of 400 nN from (1). This exceeds all of our experimentally observed critical buckling loads, including that of Figure 3a (180 nN).<sup>35</sup> This precludes both Euler and kinking (Euler buckling is needed to precede kinking) as the mechanisms for the distinct drop in force. On the basis of these unreasonable values for critical Euler buckling loads and the reasonable values obtained for critical symmetric shell buckling strains, we propose symmetric shell buckling as the cause of the instability and the subsequent negative stiffness in the force–displacement plots. As a side note, this special MWCNT/F configuration and the employment of AFM in normal force mode provide a viable alternative to determine a MWCNT/F's  $E$ , provided more care can be taken to isolate it and determine its dimensions (probably via SEM). This method can be easily extended to other vertically aligned nanostructures, e.g., nanowires.<sup>25,35</sup>

In light of the above discussion we propose a hypothetical schematic of the configurations of the MWCNT/F during loading (Figure 3b). There is ambiguity in regions 5 and beyond where severe buckling, bending, and interaction with the substrate occur. A complete understanding of the critical buckling load of long and thick MWCNTs, as well as the post-shell-buckled regimes is still lacking and more studies must be carried out.

In summary, we have shown that the buckling instabilities of individual MWCNTs of a wide range of aspect ratios under axial compression can be captured by the AFM. MWCNTs exhibit either extended elastic Euler buckling (for large aspect ratios) or brief Euler buckling followed by kinking (for moderate aspect ratios). Continuum theory provides excellent fits to the Euler buckling regime when fixed-hinged boundary conditions are used and eccentric loading and an initial imperfection (i.e., a transversely deflected shape) are accounted for. For smaller aspect ratio MWCNT/Fs, we attribute instabilities to elastic symmetric shell buckling. In all cases, the behavior is observed to be reversible and repeatable. Both kinking and symmetric shell buckling exhibit sharp drops in force with increasing axial strain. This incremental negative stiffness behavior, observed reproducibly here for the first time, opens up the possibility of harnessing the resilient mechanical properties of MWCNTs for novel composites and possibly as nanoswitches in nanoelectromechanical systems.<sup>36</sup>

**Acknowledgment.** The authors acknowledge the financial support of NSF under Grant #CMS-0136986. We thank Dr. Alex Kvit for expert assistance with the TEM.

**Supporting Information Available:** Details of the derivation of the equations used in the curve fits as well as explanation of mechanics terms used. This material is available free of charge via the Internet at <http://pubs.acs.org>.

## References

- (1) Iijima, S. *Nature* **1991**, *354*, 56.
- (2) Falvo, M. R.; Clary, G. J.; Taylor, R. M., II; Chi, V.; Brook, F. P., Jr.; Washburn, S.; Superfine, R. *Nature* **1997**, *389*, 582.
- (3) Iijima, S.; Brabec, C.; Maiti, A.; Bernholc, J. *J. Chem. Phys.* **1996**, *104*, 2089.
- (4) Timoshenko, S. P. *Theory of Elastic Stability*; Mc-Graw Hill Book Co.: New York, 1961.
- (5) Yamaki, N. *Elastic Stability of Circular Cylindrical Shells*; North-Holland Series in Applied Mathematics and Mechanics, 27; North Holland: Amsterdam, 1984.
- (6) Pantano, A.; Boyce, M. C.; Parks, D. M. *J. Eng. Mater. Technol.* **2004**, *126*, 279.
- (7) Yakobson, B. I.; Brabec, C. J.; Bernholc, J. *Phys. Rev. Lett.* **1996**, *76*, 2511.
- (8) Zhang, C.-L.; Shen, H.-S. *Carbon* **2006**, *44*, 2608.
- (9) Garg, A.; Han, J.; Sinnott, S. B. *Phys. Rev. Lett.* **1998**, *81*, 2260.
- (10) Lakes, R. S.; Lee, T.; Bersie, A.; Wang, Y. C. *Nature* **2001**, *410*, 565.
- (11) Jaglinski, T.; Kochmann, D.; Stone, D. S.; Lakes, R. S. *Science* **2007**, *315*, 620.
- (12) Kuzumaki, T.; Mitsuda, Y. *Jpn. J. Appl. Phys.* **2006**, *45*, 364.
- (13) Lee, S. I.; Howell, S. W.; Raman, A.; Reifengerger, R.; Nguyen, C. V.; Meyyappan, M. *Nanotechnology* **2004**, *15*, 416.
- (14) Poggi, M. A.; Boyles, J. S.; Bottomley, L. A.; McFarland, A. W.; Colton, J. S.; Nguyen, C. V.; Stevens, R. M.; Lillehei, P. T. *Nano Lett.* **2004**, *4*, 1009.
- (15) Kaplan-Ashiri, I.; Cohen, S. R.; Gartsman, K.; Ivanovskaya, V.; Heine, T.; Seifert, G.; Wiesel, I.; Wagner, H. D.; Tenne, R. *Proc. Nat. Acad. Sci. U.S.A.* **2006**, *103*, 523.
- (16) Waters, J. F.; Guduru, P. R.; Jouzi, M.; Xu, J. M.; Hanlon, T.; Suresh, S. *Appl. Phys. Lett.* **2005**, *87*, 103109.
- (17) Sader, J. E.; Chon, J. W. M.; Mulvaney, P. *Rev. Sci. Instrum.* **1999**, *70*, 3967.
- (18) Lixin, D.; Arai, F.; Fukuda, T. *IEEE Int. Conf. Robotics Automation, Pt. 2* **2002**, 1477.
- (19) Yap, H. Y.; Ramaker, B.; Sumant, A. V.; Carpick, R. W. *Diamond Relat. Mater.* **2006**, *15*, 1622.
- (20) The diameters of the 16 MWCNT/CNFs are determined by TEM to range from 60 to 110 nm (average of 86 nm) and wall thicknesses range from 25 to 35 nm (average 31 nm). The aspect ratio ranges from 18 to 45 (average 35).
- (21) The force is obtained by multiplying the cantilever deflection signal (volts) with the sensitivity (nm/V) and the normal stiffness of the cantilever (N/m). The latter is obtained by the Sader method (ref 15) and the former by pressing the tip onto a clean and stiff surface prior to sample loading. The MWCNT displacement is obtained by subtracting the cantilever displacement from the sample displacement during loading (after optical interference is taken into account). The percentage error in the force calibration is ~9% (~3% from the sensitivity measurements, ~5% from the quality factor measurements, and ~1% for the measurements of the other parameters in the Sader method).
- (22) The unloading curve has been translated down by 30 nm for clarity. A total of three out of five AFM - MWCNTs exhibited this behavior.
- (23) Lake, M. S.; Georgiadis, N. *NASA Tech. Memo.* **1990**, *1*, 4174.
- (24) Yu, M.-F.; Lourie, O.; Dyer, M. J.; Moloni, K.; Kelly, T. F.; Ruoff, R. S. *Science* **2000**, *287*, 637.
- (25) Wong, E. W.; Sheehan, P. E.; Lieber, C. M. *Science* **1997**, *277*, 1971.
- (26) The sample is displaced normal to the plane of the inclined cantilever, namely at 11° from vertical, using the “x-rotate option” of the Nanoscope controller, to minimize translation of the tip relative to the MWCNT/F, and to reduce transverse forces acting on the MWCNT. See also. Cannara, R. J.; Brukman M. J.; Carpick, R. W. *Rev. Sci. Instrum.* **2005**, *76*, 53706-1. Optical interference causes the spurious effect where the trace and retrace curves are not aligned prior to contact.
- (27) Wang, L.; Hu, H.; Guo, W. *Act. Mech. Sol. Sin.* **2005**, *18*, 123.
- (28) Yap, H. W.; Lakes, R. S.; Carpick, R. W. In preparation.
- (29) Ru, C. Q. *Phys. Rev. B* **2000**, *62*, 9973.
- (30) Ru, C. Q. *J. Appl. Phys.* **2001**, *89*, 3426.
- (31) Cumings, J.; Zettl, A. *Science* **2000**, *289*, 602.
- (32) The lengths of these MWCNT/Fs exhibiting shell buckling vary from 1100 to 1900 nm (average 1437 nm) and the normal stiffnesses from 2.40 to 14.84 N/m (8.48 N/m). The critical buckling strains range from 0.47 to 3.20 % (average 1.68 %) and critical buckling loads from 91 to 220 nN (average 139 nN).
- (33) Wang, C. Y.; Ru, C. Q.; Mioduchowski, A. *J. Appl. Mech.* **2004**, *71*, 622.
- (34) Tu, Z.-C.; Ou-Yang, Z.-C. *Phys. Rev. B* **2002**, *65*, 233407.
- (35) Song, J. H.; Wang, X. D.; Reido, E.; Wang, Z. L. *Nano Lett.* **2005**, *5*, 1954.
- (36) Chang, T.; Hou, J.; Guo, X. *Appl. Phys. Lett.* **2006**, *88*, 211906.

NL062763B